PHYSICAL REVIEW B **94**, 024426 (2016)

Thermal spin injection and interface insensitivity in permalloy/aluminum metallic nonlocal spin valves

A. Hojem, D. Wesenberg, and B. L. Zink
Department of Physics and Astronomy, University of Denver, Denver, Colorado 80208, USA
(Received 3 March 2016; published 21 July 2016)

We present measurements of thermal and electrical spin injection in nanoscale metallic nonlocal spin valve structures. Informed by measurements of the Seebeck coefficient and thermal conductivity of representative films made using a micromachined Si-N thermal isolation platform, we use simple analytical and finite-element thermal models to determine limits on the thermal gradient driving thermal spin injection and calculate the spin-dependent Seebeck coefficient to be $-0.5\ \mu\text{V/K} > S_s > -1.6\ \mu\text{V/K}$. This is comparable in terms of the fraction of the absolute Seebeck coefficient to previous results, despite dramatically smaller electrical spin injection signals. Since the small electrical spin signals are likely caused by interfacial effects, we conclude that thermal spin injection is less sensitive to the ferromagnetic/nonmagnetic interface, and possibly benefits from the presence of oxidized ferromagnets, which further stimulates interest in thermal spin injection for applications in sensors and pure spin current sources.

DOI: 10.1103/PhysRevB.94.024426

I. INTRODUCTION

The nonlocal spin valve (NLSV), also called a lateral spin valve or spin accumulation sensor, plays an essential role in modern spintronics because of the unique ability to separate charge current from pure spin current [1–5]. The NLSV is formed from two ferromagnetic (FM) nanowires connected by a nonmagnetic (NM) channel material with a length L on the order of the spin diffusion length. As shown schematically in Fig. 1(a), when a (charge) current I is driven from the left FM contact and extracted from the nearby end of the NM channel, the spin polarization of the electrons flowing into the channel causes a transfer of angular momentum, or spin, into the NM. This spin accumulation diffuses, decaying exponentially with distance with a spin diffusion length λ_{NM}. Note that in the ideal case no charge current is present in the NM channel where the spin accumulation leads to a pure spin current. Because of the difference in chemical potential for up and down spins, the potential difference V_{NLE} measured between the right FM contact and the right side of the NM channel depends on the relative alignment of the magnetization in the two FM contacts. Here the subscript NLE specifies the nonlocal voltage under conditions of electrical spin injection. Dividing V_{NLE} and I in this nonlocal geometry gives the nonlocal resistance resulting from electrical spin injection, R_{NLE}, which then has the dependence on applied magnetic field, H, shown in Fig. 1(b). This electrically driven NLSV allows powerful probes of spin injection, spin accumulation, and spin transport in a wide variety of material systems [6,7].

Despite decades of study, spin transport and injection even in supposedly simple metallic systems still holds open questions and surprising results, including the role of size and material effects and the nature of the injection mechanisms [8–10]. These open questions become more urgent as industrial use of NLSV sensors for demanding magnetic field sensing applications such as read heads in magnetic recording rapidly approaches reality [11]. Recently, thermal effects on the NLSV have proven a critical area of study, with some authors suggesting that the dominant physics driving the background resistance of the NLSV originates in thermoelectric effects [12–14], and others observing that significant Joule heating plays an important role in spin injection [15,16]. A few groups have even shown that spin accumulation and transport in a metallic NLSV is possible by driving heat current, rather than charge current [15,17–22]. Such a thermal injection is shown schematically in Fig. 1(c), where current is passed only through the FM contact in order to provide a local heat source at the FM/NM interface. If the resulting thermal gradient generates a spin accumulation in the NM and resulting spin current in the channel, the potential difference V_{NLT} shows a characteristic switching pattern similar to Fig. 1(b). Here the subscript NLT specifies a nonlocal voltage under conditions of thermal spin injection. This thermal generation of pure spin current, usually called the spin-dependent Seebeck effect (SDSE) [23], is still largely unexplored, and often difficult to quantify due to the need to accurately determine the thermal gradient in nanoscale structures. There is a great deal of interest in the SDSE for applications in sensors and as a source for pure spin currents in possible spin-based logic [24–28], as well as for its role in spin-torque switching in response to fast or ultrafast laser fluence [22].

In this paper we present measurements of thermal and electrical spin injection and transport in all-metallic NLSVs made using permalloy (Py, the Ni-Fe alloy with 80% Ni) FM and aluminum NM. In addition to quasi-dc measurements using the equivalent of the lock-in amplifier techniques common in the field, we fully characterize the voltage-current characteristics of the NLSV in both electrical and thermal spin injection configurations. As discussed in detail below, this allows description of each device using a simple analytic thermal model that includes Joule heating and Peltier heating or cooling. With knowledge of the thermal conductivity and Seebeck coefficients of representative films that we measure using our technology for thin-film thermal measurements [29–35], we determine an upper limit on the thermal gradient driving spin injection without recourse to complicated simulations or assumptions of bulk thermal properties. We also use a 2d finite-element approach based on purely diffusive heat flow, though again informed by measured values of thermal conductivity and Seebeck coefficients, to approach a more

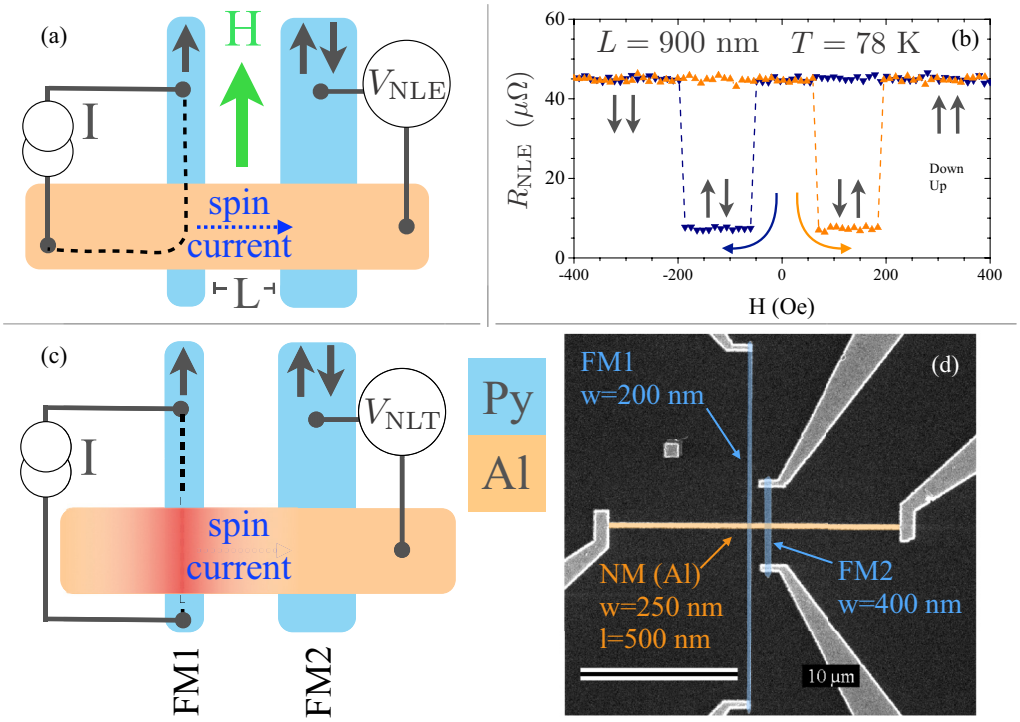

FIG. 1. (a) Schematic layout of the NLSV under electrical spin injection, where a large charge current driven through a FM nanowire creates a spin accumulation and pure spin current in a NM channel that is detected with a second FM. (b) The nonlocal resistance $R_{NLE} = V_{NLE}/I$ for a $L = 900$ nm device at 78 K, where the relative alignments of the two FM contacts are indicated with paired arrows. (c) Thermal spin injection is achieved by passing current I only through FM1, creating a thermal gradient at the NM/FM interface that injects spin into the NM. (d) False-color SEM micrograph of the nanoscale circuit defining the NLSV. Sizes given indicate the designed widths of nanowires; measured geometries appear in Table I.

realistic estimate of the thermal gradient and the SDSE. The resulting SDSE coefficient for the Py/Al system at 78 K that we report here is smaller in absolute value than previous reports using typical ferromagnets, though very comparable as a fraction of the absolute Seebeck coefficient [15,17] despite a very low efficiency of electrical injection. This suggests that thermal spin injection is far less sensitive to the nature of the FM/NM interface than its electrical counterpart and motivates broader study of the materials dependence and interface dependence of thermal spin injection.

II. EXPERIMENT

A. Device fabrication

We fabricate NLSVs via a two-step e-beam lithography liftoff process. Starting with silicon-nitride-coated 1 cm × 1 cm Si chips with prepatterned Au or Pt leads and bond pads, we spin an ≈150 nm thick layer of PMMA that is baked for 30 min at 180 °C. After exposure of the FM nanowire pattern using a 40 kV SEM with the NPGS package [36] at a dose of ∼600 μC/cm^2 and a 45 s development in a 1:3 MIBK:IPA solution, we deposited 100 nm of Py from a single Ni-Fe alloy source in a load-locked UHV e-beam evaporation system at growth rates of ∼0.15 nm/s. After removal of the resist, we spin an ≈380 nm PMGI spacer layer that is baked at 250° for 30 min, followed by an ≈100 nm thick PMMA imaging layer. After e-beam exposure of the NM channel and lead pattern and a two-step development (1:3:MIBK for 45 s, followed by a 35 s soak in 1:30 solution of 2% TMAH:IPA to form the undercut in the PMGI), we deposited a 110 nm Al layer in a HV e-beam evaporation system at 0.2–0.5 nm/s using a water-cooled stage after a 2 minute, 50 W, −580 V RF clean process in 10 mT of Ar intended to desorb moisture from the exposed FM surface (to promote adhesion during liftoff) and potentially remove the native oxide formed on the Py nanowires. We then remove the PMGI/PMMA resist stack via a 45 min soak in 80 °C MicroChem Remover PG. A scanning electron micrograph showing an example NLSV is shown in Fig. 1(d).

B. Transport measurements

Measurements are carried out after bolting the NLSV chip to a fully radiation-shielded gold-coated high-purity Cu sample mount installed in a sample-in-vacuum LN2 cryostat. An open bore split-coil electromagnet allows application of fields in excess of 1000 Oe in the plane of the chip. For the measurements described here the field is applied as shown in Fig. 1(a). Simple resistance or nonlocal resistance measurements are made using the "delta mode" function of a linked Keithley 2128a nanovoltmeter and 6220 high-precision current source. This measurement is functionally equivalent to a first-harmonic lock-in amplifier measurement [37]. We determine IV characteristics of the NLSV in various configurations by numerically integrating differential conductance

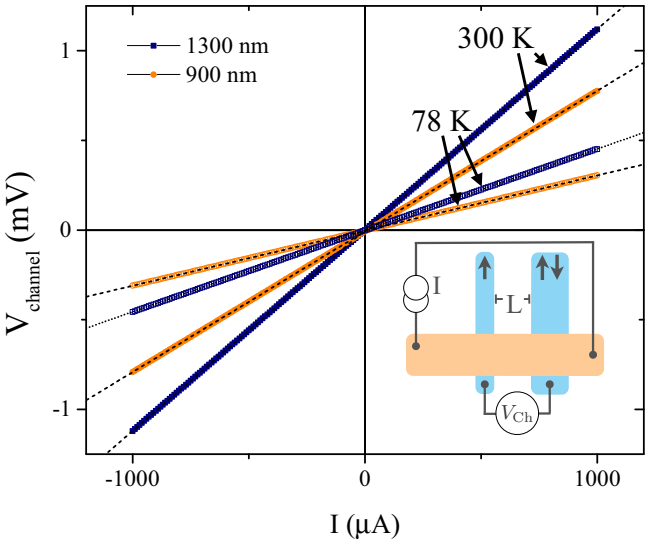

FIG. 2. V_{channel} vs I characteristics for the NM channel (contacts made as shown schematically in the inset) are highly linear across the entire range of applied I in contrast to both the three-terminal contact resistance [Fig. 6(e)] and nonlocal resistance measurements [Figs. 5(a) and 6(c)]. Measurements for two NLSVs are shown for two temperatures. Dashed lines show linear fits.

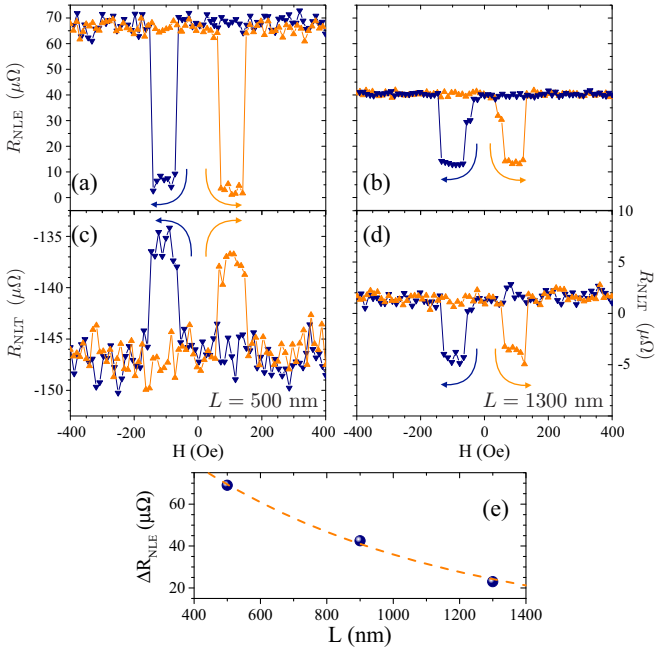

FIG. 3. Nonlocal resistance signals $R_{\text{NLE}} = V_{\text{NLE}}/I$ in electrical [(a) and (b)] and $R_{\text{NLT}} = V_{\text{NLT}}/I$ in thermal [(c) and (d)] spin injection for both 500 nm and 1300 nm nominal FM spacing. (e) The electrical spin signal ΔR_{NLE} vs L with the fit to the 1d spin diffusion equation. This fit gives $\lambda_{\text{NM}} = 760 \pm 50$ nm.

measurements made with the same system [38]. Figure 2 shows an example IV measurement of the NM channel for the $L = 900$ nm and $L = 1300$ nm devices at both $T = 78$ K and 300 K. Since no FM/NM couple is in the current path in this measurement, no thermoelectric contributions are expected and indeed V_{channel} is highly linear for the entire range of applied I, as seen by the excellent agreement with linear fits shown with dashed lines.

After all measurements are completed on a NLSV, we measure the FM and NM film thicknesses via AFM contact profilometry and the actual lateral geometry of the nanowires using SEM micrographs (see Table I). For the devices described here, this revealed somewhat wider NM channels than intended, with widths reaching 400–450 nm. These measured values are used wherever geometry is needed in model calculations.

III. RESULTS

Figure 3 shows the nonlocal resistance as a function of applied field for two NLSVs with different FM spacing, L. Panels (a) and (b) result from electrical spin injection using a bias current of $I = 1$ mA [Fig. 1(a)], while in panels (c) and (d) current ($I = 2$ mA) flows only in the FM, causing no net charge current to pass into either arm of the NM channel, but heating the FM such that a heat current forms at the FM/NM interface. The characteristic switching clearly shows that this heating generates a spin accumulation in the NM channel that is detected after diffusing to the location of FM2. Note, however, that this quasi-dc R measurement is sensitive to terms linear in I, where heating effects are proportional to I^2. The apparent sign change in $\Delta R_{\text{NLT}} = R_{\text{NLT}}(\uparrow\uparrow) - R_{\text{NLT}}(\uparrow\downarrow)$ is peculiar, but as is discussed in more detail below does not indicate a sign change in the SDSE.

As shown in Fig. 3(e), we use $\Delta R_{\text{NLE}} = R_{\text{NLE}}(\uparrow\uparrow) - R_{\text{NLE}}(\uparrow\downarrow)$ to determine the spin diffusion length in the Al, λ_{NM}. As discussed further below, this device does not clearly meet the criterion for any of the three limits typically used to analyze signals in NLSVs, but is closest to the case of tunnel contacts. In this tunneling limit, the form of the 1d spin diffusion equation is [39]

$$\Delta R_{\text{NLE}} = P_I^2 \mathcal{R}_{\text{NM}} e^{-L/\lambda_{\text{NM}}}, \tag{1}$$

and this equation can safely be used at least to determine λ_{NM}. The fit shown by the dashed line in the Fig. 3(b) inset gives $\lambda_{\text{NM}} = 760 \pm 50$ nm, which is in line with previous results for Al [9,40].

To better understand the signal size in this series of Py/Al NLSVs, in Fig. 4(a) we compare the experimental ΔR_{NLE} as a function of FM separation, L, on a semilog plot to expectation of various models described by Takahashi and Maekawa [39]. If spin-flip scattering at the interfaces is ignored, the NLSV

TABLE I. NLSV geometries as measured by scanning electron micrography. Each dimension has an estimated error of 30 nm.

Device	L	w_{FM_1} (nm)	w_{FM_2} (nm)	w_{NM} (nm)
500 nm	475	190	400	510
900 nm	850	230	415	485
1300 nm	1260	225	425	460

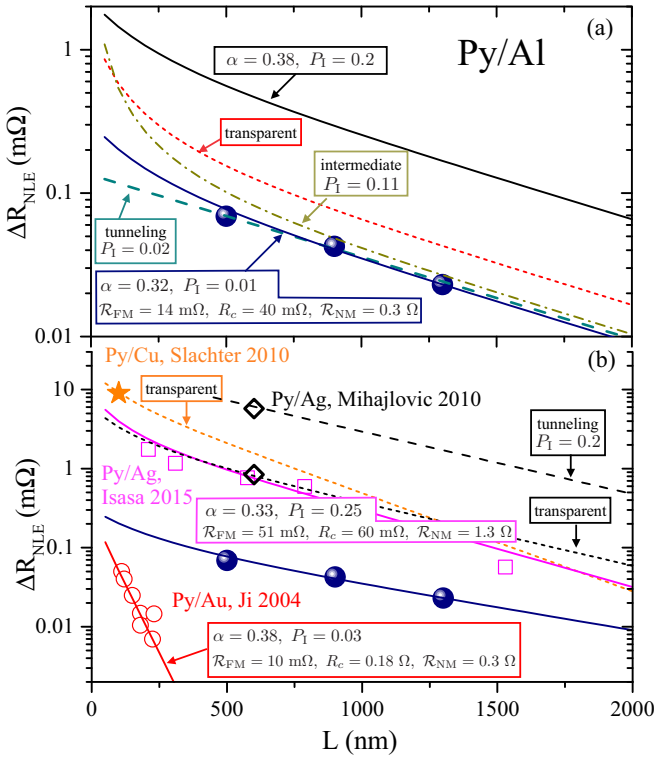

FIG. 4. (a) Comparison of electrically driven spin signal $\Delta R_{\rm NLE}$ (blue spheres) to various models based on the 1d spin diffusion equation [39]. Matching of the electrical signal is only possible using a strongly reduced value of interfacial spin polarization, regardless of the model employed. (b) Comparison of $\Delta R_{\rm NLE}$ reported here (blue spheres) to similar Py-based NLSVs with various NM channels [3,15,44,45]. In each case the lines represent a 1d spin diffusion model that explains the signal size. Relevant parameters and spin resistances are also given. Note especially the large signal that matches predictions of the transparent interface model for the Py/Cu device originally used to observe the SDSE [15]. NLSVs used in this study have much reduced electrical signal, but maintain the same thermally driven spin signal.

signal is predicted to follow

$$\Delta R_{\rm NLE} = 4\mathcal{R}_{\rm NM} e^{-L/\lambda_{\rm NM}} \prod_{i=1}^{2}\left(\frac{P_I \frac{R_i}{\mathcal{R}_{\rm NM}}}{1-P_I^2} + \frac{\alpha \frac{\mathcal{R}_{\rm FM}}{\mathcal{R}_{\rm NM}}}{1-\alpha^2}\right) \times \left[\prod_{i=1}^{2}\left(1 + \frac{2\frac{R_i}{\mathcal{R}_{\rm NM}}}{1-P_I^2} + \frac{2\frac{\mathcal{R}_{\rm FM}}{\mathcal{R}_{\rm nm}}}{1-\alpha^2}\right) - e^{-2L/\lambda_{\rm NM}}\right]^{-1}. \quad (2)$$

Here R_i is the contact resistance of the ith FM/NM interface, $\alpha = (\sigma_\uparrow - \sigma_\downarrow)/(\sigma_\uparrow + \sigma_\downarrow)$ is the spin polarization of the FM nanowire, $P_I = (G_\uparrow - G_\downarrow)/(G_\uparrow + G_\downarrow)$ is the spin polarization of the interfacial current with $G_\uparrow$ ($G_\downarrow$) giving the interfacial conductance of the two spin channels, and

$$\mathcal{R}_{\rm FM} = \rho_{\rm Py}\lambda_{\rm Py}/w_{\rm FM}w_{\rm nm} \quad (3)$$

and

$$\mathcal{R}_{\rm NM} = \rho_{\rm Al}\lambda_{\rm NM}/t_{\rm NM}w_{\rm NM} \quad (4)$$

are the spin resistances of the ferromagnet and normal metal, respectively. Takahashi and Maekawa use reduction of the P_I term to phenomenologically take interfacial spin-flips into account, though others have considered this issue directly [41].

Equation (2) is commonly simplified for the three limits often, but not always, relevant to particular NLSV fabrication techniques. It is also common to assume a single contact resistance value for both FM/NM junctions, $R_i = R_c$. With this notation the three limits are the transparent limit, where $R_c \ll \mathcal{R}_{\rm FM}$:

$$\Delta R_{\rm NLE} = 4\frac{\alpha^2\mathcal{R}_{\rm FM}^2}{(1-\alpha^2)^2\mathcal{R}_{\rm NM}} \frac{e^{(-L/\lambda_{\rm NM})}}{\left[1+\frac{2\mathcal{R}_{\rm FM}}{(1-\alpha^2)\mathcal{R}_{\rm NM}}\right]^2 - e^{(-2L/\lambda_{\rm NM})}}, \quad (5)$$

the intermediate limit ($\mathcal{R}_{\rm NM} \gg R_c \gg \mathcal{R}_{\rm FM}$):

$$\Delta R_{\rm NLE} = 4\frac{P_I^2}{\left(1-P_I^2\right)^2}\frac{R_c^2}{\mathcal{R}_{\rm NM}}\frac{e^{-L/\lambda_{\rm NM}}}{1-e^{-2L/\lambda_{\rm NM}}}, \quad (6)$$

and the tunneling limit, $R_c \gg \mathcal{R}_{\rm NM}$, given in Eq. (1) above.

Following common practice, we estimate the contact resistance from a transport measurement as shown schematically in the inset to Fig. 6(e). The linear slope of this measurement provides R_c for this set of devices. Despite the RF clean step between the FM and NM depositions, we measure a fairly large contact resistance, such that at 78 K, $R_c \approx 40$ mΩ. The value of the contact resistance area product, $R_c A = 4$ mΩ μm^2 (from the $L = 1300$ nm NLSV), is roughly an order of magnitude higher than seen in transparent contacts [9], and on par with the lowest values seen in MgO tunnel barriers capable of strongly enhancing $\Delta R_{\rm NLE}$ [42]. However, in our devices $\mathcal{R}_{\rm FM} \approx 14$ mΩ and $\mathcal{R}_{\rm NM} \approx 0.28$ Ω. This indicates that $\mathcal{R}_{\rm NM} > R_c > \mathcal{R}_{\rm FM}$, meaning that the NLSV is far from the limit of transparent interfaces defined by $R_c \ll \mathcal{R}_{\rm FM}$. Since R_c is only $\approx 2\mathcal{R}_{\rm NM}$, these devices do not belong to any of the simpler limits, though they are nearest to the intermediate limit. In Fig. 4(a) we compare the predictions of the model for our geometry and resistances. Though reports vary, for Py/Al NLSVs, $\alpha = 0.38$ and $P_I = 0.2$ are fairly common values. The solid black line in Fig. 4(a) gives the expected $\Delta R_{\rm NLE}$ calculated from Eq. (2) using these parameters and our measured geometry and R_c. Note that this calculation is nearly linear above 500 nm, suggesting single exponential behavior as seen in the tunneling model. However, as is the case for similar predictions of the transparent and intermediate models [Eqs. (5) and (6)], the theory assuming no interfacial spin-flip scattering predicts much larger $\Delta R_{\rm NLE}$ than we observe. The full theory does match the measured data well if P_I is strongly reduced to $\approx$0.01, as shown in the solid navy blue curve. Note that we must also somewhat reduce α to match the observed values, and here we choose $\alpha = 0.32$, a reduction of 15% motivated by a similar reduction in M_s for Py grown from this source in our chamber [43]. We clarify that these predictions are not fits and there are obviously not enough data here to determine all the possible parameters. We can also roughly match the measured data using the intermediate model, but only using a significantly reduced $P_I = 0.11$. We interpret this reduced signal as evidence of a high degree of interfacial spin-flip scattering in our NLSVs. As noted above, the simple

single-exponential tunneling model can also fit the data well with a low value of $P_I = 0.02$. Such a fit is more convenient, if less obviously physical than use of the full equation where the spin polarization of the FM itself provides the difference in spin potentials that determine the signal, with a significant drop of electrochemical potential at the interfaces that has very low spin polarization and does not increase the signal. A fit with poor χ^2 and large error bars on parameters is also possible using the transparent equation, though there is little physical justification for use of this model considering the relative values of R_c and $\mathcal{R}_{\rm FM}$.

Figure 4(b) compares our NLSV to a range of other devices reported in the literature using Py ferromagnetic elements. Perhaps most importantly, we first point out the large signal size reported by Slachter *et al.* in the initial report of the SDSE indicated by the orange star [15]. The transparent spin diffusion model prediction of this signal is also shown as a dashed line. This prediction is at least 10 times greater than the values we measure for all L. We also compare our results to some of the earliest reports on Py/Au devices, where similarly small overall signal size was observed at 10 K using a Au normal metal channel [3]. This set of devices also showed a pattern of contact and spin resistance similar to that of our NLSV, and can be explained with the same reduction of P_I as a result of likely interfacial spin-flip scattering. One can also fit the tunneling equation to the data from Ji *et al.* [3], which gives a very low value of $P_I = 0.03$. Because of the short $\lambda_{\rm NM}$ of Au in comparison to Cu or Al, the transparent model can also be tuned to match the Ji data, though again the contact resistance is far higher than $\mathcal{R}_{\rm FM}$ and there is little physical justification for use of the transparent model.

Figure 4(b) also compares data from Isasa *et al.* on polycrystalline Ag channels where the full equation is the only reasonable match for the signal size [44], as well as for a Py/Ag NLSV that was exposed to atmosphere over a long period of time by Mihaijlovic *et al.* [45]. This exposure caused diffusion of oxygen through grain boundaries in the Ag overlayer, allowing increased oxidation of the underlying Py. In this case, the additional oxide increased $\Delta R_{\rm NLE}$ dramatically, such that the device that matched expectations of the transparent limit converged to the tunneling prediction (though no measurements of contact resistance were included so the match to models remains approximate).

Though we cannot truly specify the physical mechanism responsible for low electrically driven spin signals and low P_I in the NLSV we used here, it is clear that oxidation of the Py nanowires followed by the RF sputter-clean before Al deposition resulted in an imperfect interface. Here some amount of the native oxide most likely remains, and the resulting disordered magnetic environment scatters spins as they are electrically driven through the interface into the NM.

Figure 5 details the extraction of spin accumulation signals from the full IV characteristics measured in both electrical

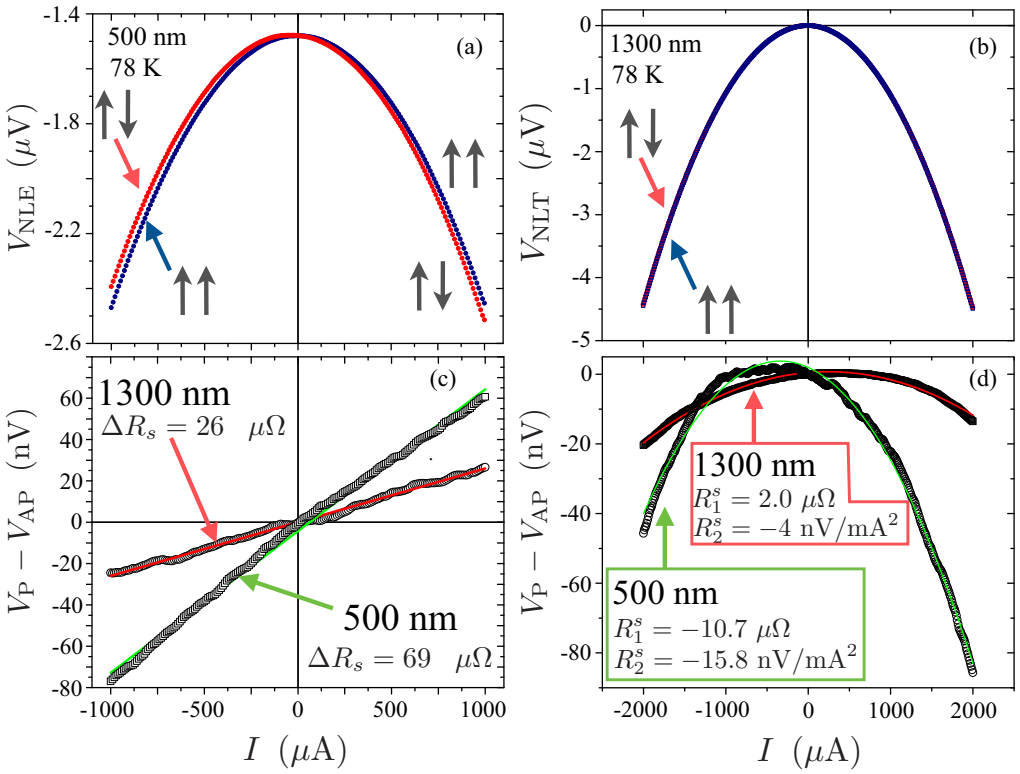

FIG. 5. (a) IV characteristic for the electrical spin injection configuration [Fig. 1(a)] measured separately for parallel and antiparallel states of the FM nanowires for the $L = 500$ nm device at 78 K. (b) The corresponding IV characteristic for the thermal spin injection configuration [Fig. 1(c)]. (c) Subtraction of the parallel and antiparallel curves in (a) gives the highly linear response of electrical spin injection, while the corresponding subtraction for thermal injection yields a spin signal dominated by the I^2 term indicating thermal generation of a spin accumulation in the NM. In both (c) and (d), data for both $L = 500$ nm and $L = 1300$ nm are shown. Fitted values of spin signal are also shown.

and thermal spin injection configurations. Figure 5(a) plots V_{NLE} vs I for $L = 500$ nm at 78 K measured for two different fields, chosen based on the R_{NLE} vs H patterns in Fig. 3(a) to give the parallel (labeled $\uparrow\uparrow$) and antiparallel ($\uparrow\downarrow$) states of the FM nanowires. Both curves show obvious terms $\propto I$ and $\propto I^2$. The striking nonlinearity is a clear indication of the importance of thermal and thermoelectric effects in this NLSV. However, subtracting the two curves gives the very linear response shown in Fig. 5(c) for both $L = 500$ nm and $L = 1300$ nm, where the slope matches the spin signal seen in R_{NLE} vs H. Figures 5(b) and 5(d) show similar plots for thermal spin injection (V_{NLT}) measured at the same temperature over a wider I range. As expected V_{NLT} is predominantly $\propto I^2$, and the difference between parallel and antiparallel configurations [Fig. 5(d)] retains a large $\propto I^2$ component. Lines in Fig. 5(d) are fits to $V_{\mathrm{P-AP}} = R_1^s I + R_2^s I^2$. As discussed further below, the R_2^s provides the same information as the second-harmonic lock-in signal in previous work [15], and is the evidence of thermally generated spin accumulation in the NLSV. The physics of the R_1^s term is less clear, though this term was also seen in the original report of the SDSE [15]. In fact, the size of R_1^s and R_2^s shown in Fig. 5(d) for $L = 500$ nm is nearly the same as the results in [15]. However, this does not necessarily imply a similar SDSE coefficient, since the thermal profile in the NLSV must be determined and will certainly depend on the detailed geometry and materials in each device. We also point out that the difference in sign in R_1^s between the 500 nm and 1300 nm devices entirely explains the sign change of ΔR_{NLT} apparent in Figs. 3(c) and 3(d) and clarifies that this is not related to the SDSE. Recent electrical injection experiments in the wiring configuration of Fig. 1(b) for a Py/Cu NLSV with Al_2O_3 tunnel barriers showed a spin accumulation signal that was interpreted as evidence of a nonuniform spin injection across the contact [46]. A similar mechanism could well explain our R_1^s, but further study is required to conclusively discuss this.

IV. DISCUSSION

Accurately determining the thermal gradient generated in any nanoscale metallic device is a serious challenge. Even if complicated 3d finite-element analysis (FEM) is used, having accurate values of thermal properties for the thin-film constituents of the devices is important, and the role of interfaces for electron, phonon, and spin transport is difficult to quantify without great effort [47,48]. Furthermore, typical codes describe only diffusive heat transport, ignoring ballistic or quasiballistic phonon transport that is known to play a role in nanoscale metallic features on insulating substrates [49]. In fact the previously common view that only phonons of quite short wavelength and mean-free path dominate heat transport in bulk materials at room temperature is now understood to be incorrect, with more and more quantitative measurements showing large contributions to heat flow from parts of the phonon spectrum ignored in typical FEM simulations [34,50–54]. These issues suggest that truly quantitative determination of the SDSE coefficient will be challenging and some level of disagreement between experimental groups should be expected, a situation familiar to the spintronics community.

We therefore clarify that the main result of this study requires no complicated or controversial calculations of thermal gradients. First consider that the spin signal due to electrical spin injection in the NLSV first used for the SDSE measurement by Slachter *et al.* [15] was [as shown in Fig. 4(b) above] $\Delta R_{\mathrm{NLE}} \approx 10$ mΩ, where the thermal injection signal as discussed earlier was $R_2^s = -16$ nV/mA^2. In the NLSV devices described here we achieved the same thermal spin signal R_2^s despite an electrical spin signal of only $\Delta R_s \approx 70$ μΩ, a factor of more than 100 smaller. We can also use a simple 1d Valet-Fert model for spin diffusion to make a more fair comparison of spin accumulation at the injection site between devices and injection techniques. This suggests that Slachter *et al.*'s $L = 100$ nm asymmetric NLSV where ion milling was used to remove Py oxide at the interfaces showed thermal spin accumulation of <0.2% of electrical spin accumulation at the same applied current. Our NLSVs, where Py oxide likely remains at the interface, show similar thermal spin accumulation but dramatically smaller electrical spin accumulation so that the ratio is >15%. As discussed further below, this suggests that thermal spin injection is much more tolerant of imperfect interface quality, and in fact may be enhanced by the presence of an oxidized Py layer.

We now consider two techniques for estimating the thermal gradient driving the SDSE in our NLSVs. The first is a simple analytic technique using the two-body thermal models shown in Figs. 6(a) and 6(b). Here we assume the two FM/NM junctions equilibrate to two different temperatures in steady state, T_1 and T_2, that both junctions are connected to thermal ground (the substrate held at T_0) via the same thermal conductance K_{sub}, and that heat can flow between the two junctions via thermal conductance K_{nm}. This model is shown schematically for electrical spin injection in Fig. 6(a). Note that truly ascribing physical meaning to the parameters in this simple model is difficult. For example one would normally expect that the NM channel in a typical NLSV would be coupled to the bath (substrate) with approximately the same thermal conductance as the junctions, though all these features are on the size scale where decoupling from the phonons responsible for heat-sinking the metal structures can lead to larger heating effects and counterintuitive behavior [49].

As already noted by other groups [12,14,16], when current is driven into the injector FM and out of one arm of the NM channel, Joule heating in this current path is accompanied by either cooling or heating due to the Peltier effect. Whereas Joule heating, $P_{\mathrm{J}} = I^2 R_{\mathrm{eff}}$, is always positive, the Peltier term, $P_{\Pi_{\mathrm{rel}}} = I\,\Pi_{\mathrm{rel}}$, is either positive or negative. The sign of the Peltier term depends on the direction of applied current, the geometric arrangement of the two metals with respect to this current flow, and the difference in the absolute Peltier coefficients of the two materials (written here simply as the relative coefficient Π_{rel}). Furthermore, via Onsager reciprocity [33,55], $\Pi_{\mathrm{rel}} = S_{\mathrm{rel}} T_0$ with the relative Seebeck coefficient S_{rel}, where we use the substrate temperature since deviation in T even by several kelvins makes a negligible change in the Peltier power at the T studied here.

The schematics in Figs. 6(a) and 6(b) for electrical and thermal spin injection, in addition to a three-terminal contact

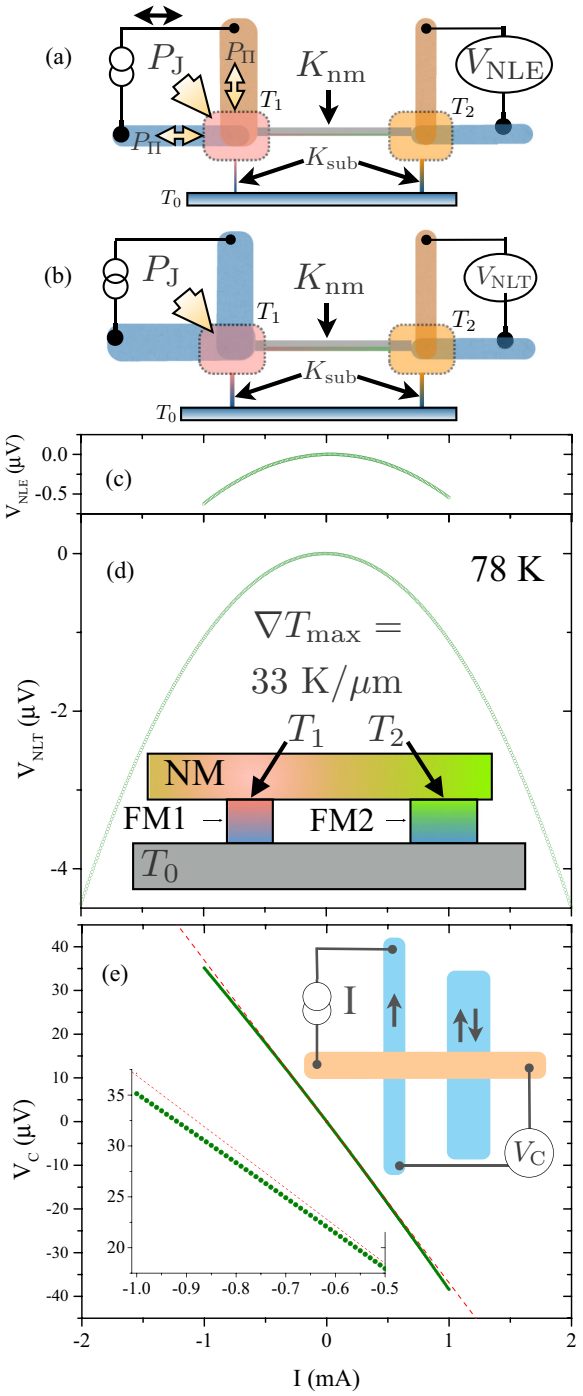

FIG. 6. (a)–(b) Two-body thermal models used to analytically model the T profile in the devices. (c)–(d) Resulting IV curves show significant curvature as a result of heating and thermoelectric effects. Data are shown for the $L = 1300$ nm NLSV at 78 K, but similar curvature is seen at room T and for other devices. Inset: The simplified thermal profile used to estimate a maximum possible ∇T of 33 K/micron from our data. (e) The three-terminal contact resistance (shown schematically in upper inset) IV characteristic shows small but clearly measurable nonlinearity (lower inset).

resistance measurement shown in Fig. 6(e) with voltage V_C, lead to a coupled system of equations that can be compared to fits of the full IV characteristics in the configurations shown in Figs. 1(a), 1(b), and 6(e). Each of these measurements contains terms proportional to I and to I^2 and are fitted to

$$V_{NLE} = A_1 I + A_2 I^2, \tag{7}$$

$$V_{NLT} = B_1 I + B_2 I^2, \tag{8}$$

$$V_C = C_1 I + C_2 I^2. \tag{9}$$

Collecting terms in the corresponding thermal model that are proportional to I and I^2 and solving these systems of equations yields expressions for the thermal parameters (as shown in the Appendix). With certain assumptions listed below we can then calculate the temperature difference between the heated region of junction 1 and the substrate in thermal spin injection, ΔT_1^t. This is the critical value needed to calculate the SDSE coefficient, S_s. First we assume that the parameter K_{nm} is given by the thermal conductance of the normal metal nanowire itself (ignoring any heat transported by the underlying substrate) and use the Wiedemann-Franz law to determine this K_{nm} from the measured resistance of the channel, R_{nm},

$$K_{nm} = \frac{L_{Al} T_0}{R_{nm}}. \tag{10}$$

Here we take the value of the Lorenz number, $L_{Al} = 2.0 \times 10^{-8}$ WΩ/K^2, from a measurement of a similar Al thin film made using our micromachined thermal isolation platform [35]. Next we assume that both the injection and detection FM/NM arms of the NLSV have the same value of S_{rel}. Though thermopower is often assumed to be independent of geometry, this is only strictly true in the case where thermal gradient is simply aligned with the sample and in the regime where size effects cannot play a role. Nanoscale metal features are not always in this simple limit [56,57], so our model could be improved using actual measurements of Seebeck effects in nanowires of the same dimension as used in the NLSV. Since these measurements are not possible for the current devices, we instead take a value of the relative Seebeck coefficient at 78 K again from measurements of representative films made using thermal isolation platforms.

Seebeck coefficient data are shown in Fig. 7, where we present the estimated absolute Seebeck coefficient as a function of T for both Al and Py films. These measurements are made on thin films deposited on a patterned 500 nm thick suspended silicon-nitride membrane with integrated heaters, thermometers, and electrical contacts. Application of a temperature difference $\Delta T = T_H - T_c$ generates a voltage across the film due to the Seebeck effect, V, giving the relative Seebeck coefficient, $S_{rel} = V/\Delta T = S_{abs} - S_{lead}$. Note that both measurements are made with the same lead material, so the determination of S_{abs} (which adds some uncertainty) is not necessary to determine the value needed for NLSV modeling, $S_{rel} = S_{Al} - S_{Py}$. More details about Seebeck measurements made with our thermal isolation platforms are available elsewhere [31–33,58].

With these assumptions we can write

$$K_{sub} = \left(\frac{C_2}{A_1} \frac{S_{rel} T_0}{R_{eff}^e} - 1 \right) K_{nm}, \tag{11}$$

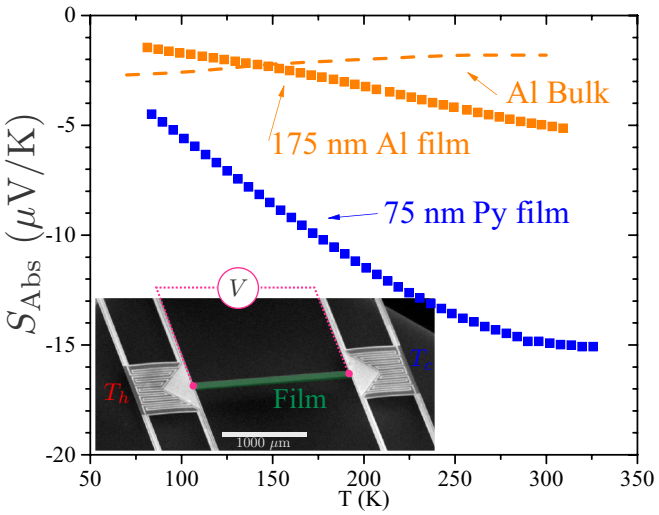

FIG. 7. Measured Seebeck coefficients for the constituent thin films vs T. Each film was deposited on a thermal isolation platform, and the measured Seebeck coefficient is relative to Cr/Pt leads. The estimated lead contribution has been subtracted here, so that this plot compares estimated *absolute* Seebeck coefficients. Inset: Scanning electron micrograph of the thermal isolation platform we use for thermal properties measurements.

where here we use $R^e_{\rm eff} = S_{\rm rel}T_0(A_2/A_1)$ for the contact resistance measurement to determine $K_{\rm sub}$. The temperature rise at the injector junction is then

$$\Delta T_1^t = \left(\frac{B_2}{S_{\rm rel}}\frac{(K_{\rm sub}+2K_{\rm nm})}{K_{\rm nm}}\right)\left[1-\frac{A_1K_{\rm sub}}{S_{\rm rel}^2T_0}\right]I^2. \quad (12)$$

The B_2 term enters from use of $R^t_{\rm eff} = S_{\rm rel}T_0(B_2/A_1)$ to account for the different effective resistance when current flows only through FM1.

ΔT_1^t for the two NLSVs for two different currents are shown in Table II, and indicate that the NLSV junctions heat by several kelvins during operation in thermal injection. The SDSE coefficient, S_s, following [15] is

$$S_s = \frac{V_s}{\nabla T \lambda_{\rm FM} R_{\rm mis}}, \quad (13)$$

where $V_s = -\mu_s/e$ is the spin accumulation at the injection junction (FM1), and $R_{\rm mis} = \mathcal{R}_{\rm NM}/[\mathcal{R}_{\rm NM} + (\mathcal{R}_{\rm FM}/1-P_I^2)]$ is always $\cong$1 for these metallic NLSVs. To estimate the SDSE coefficient, S_s, we need to determine a thermal gradient at the injection site from our temperature difference. For the analytic model we assume the highly simplified situation shown schematically in the inset in Fig. 6(d), where the temperature $T_1^t = T_0 + \Delta T_1^t$ is the effective temperature of the interface between FM and NM, and apply the 1d heat flow equation across the FM with the boundary conditions of T_0 and T_1^t, which gives a linear thermal gradient in the FM. The resulting ∇T_1^t for two applied currents is also shown in Table II, and is comparable to that calculated in other work for large I [15,17,18]. Note that this simple assumption amounts to the limit where the NM channel can only exchange heat with the top surface of each FM contact, and is most likely not physically accurate. However, it does provide an estimate for the largest absolute value of gradients possible in our structure because it ignores heat-sinking by the NM channel which will lower ∇T at the interface.

TABLE II. Fitting parameters as defined in Eqs. (7)–(9) and resulting temperature difference, and absolute values of thermal gradient from the analytic thermal model (ΔT_1^t and ∇T_1^t) and resulting lower limit on SDSE coefficient, S_s, compared to temperature difference, thermal gradient, and SDSE coefficient from FEM modeling ($\Delta T_1^{\rm FEM}$, $\nabla T_1^{\rm FEM}$, and $S_{s,\rm FEM}$). †: Value calculated from model assuming the same value of $K_{\rm sub}$ for both devices.

	500 nm	1300 nm
A_1	3.9 $\mu\Omega$	39.34 $\mu\Omega$
A_2	-0.984 V/A^2	-0.586 V/A^2
B_1	-146.95 $\mu\Omega$	-11.43 $\mu\Omega$
B_2	-1.498 V/A^2	-1.112 V/A^2
C_1		-36.76 mΩ
C_2	$-1.76^\dagger$ V/A^2	-1.66 V/A^2
ΔT_1^t (2 mA)	5.3 K	3.3 K
∇T_1^t (2 mA)	53 K/μm	33 K/μm
S_s	-0.46 μV/K	-0.53 μV/K
$\Delta T_1^{\rm FEM}$ (2 mA)	3.9 K	5.4 K
$\nabla T_1^{\rm FEM}$ (2 mA)	15 K/μm	23 K/μm
$S_{s,\rm FEM}$	-1.6 μV/K	-0.77 μV/K

The opposite limit is described by a purely diffusive heat flow model that allows exchange of energy between elements in the real geometry of the device. 3d finite-element modeling (FEM) calculations that couple the heat, charge, and spin degrees of freedom to calculate ∇T in this limit have already been demonstrated [14,15,59]. The second thermal modeling approach we take is a simple FEM calculation focusing only on the thermal degrees of freedom, and taking 2d "slices" through the device structure in critical areas. Similar 2d FEM codes have been frequently used to describe heat flow in micro- and nanomachined calorimeters [60–63]. We performed 2d FEM using a common commercially available software package [64]. This allows solution of the 2d heat flow equation (for our purposes limited to steady state):

$$\frac{\partial}{\partial x}\left(k_{\rm 2D}(x,y)\frac{\partial T(x,y)}{\partial x}\right)+\frac{\partial}{\partial y}\left(k_{\rm 2D}(x,y)\frac{\partial T(x,y)}{\partial y}\right) = P_{\rm 2D}(x,y), \quad (14)$$

where $k_{\rm 2D} = kt$ with k the thermal conductivity (in W/mK) of the constituent materials shown in Fig. 8(a) and t is a uniform thickness (here 450 nm) of the hypothetical cross section. As long as the heat flow is dominated by the bulk substrate so that in-plane thermal transport is negligible on long length scales, such a model gives a reasonable estimate of the thermal gradient at the FM/NM interface. To match our experimental conditions (sample in vacuum, with substrate clamped at the bottom to a thermal bath), we choose the Dirichlet boundary condition at the base of the Si substrate (fixing $T = 78$ K), and Neumann boundary conditions elsewhere with no radiative or convective heat flow.

Values of the thermal conductivity of the metallic nanowires are determined in the same fashion as for the analytic model (the WF law with modified L for Al and using measured values for similar thickness of Py). For the Si-N underlayer, which

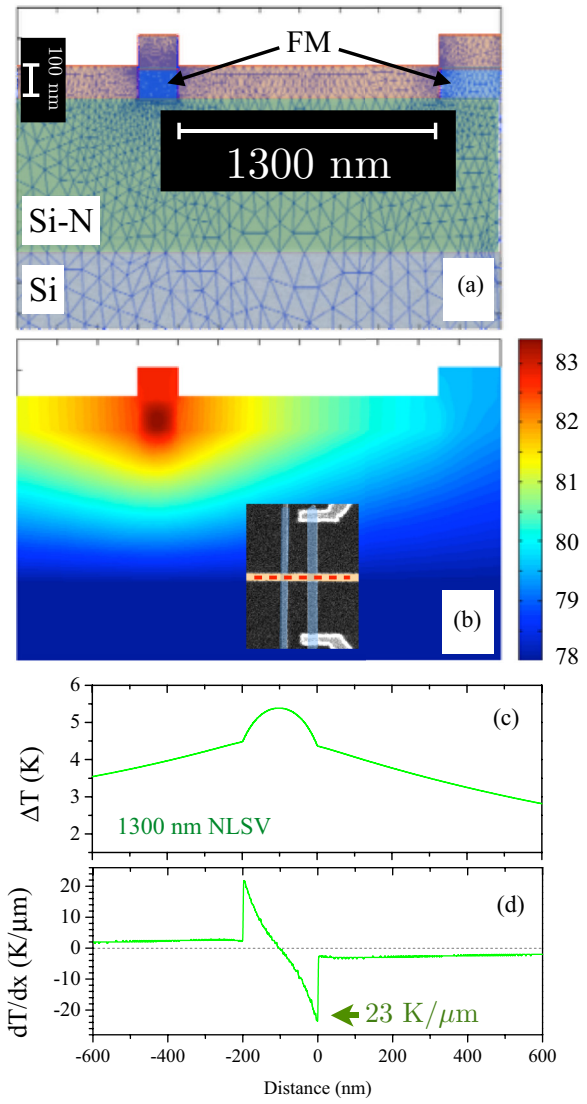

FIG. 8. (a) 2d geometry and mesh used for FEM thermal calculations. (b) Thermal profile resulting from heat dissipated in FM1 chosen to give the correct ΔT at FM2. Inset: Dashed red line shows the region of the 2d cross-sectional slice used for the FEM model. (c)–(d) Resulting T and dT/dx profiles for the $L = 1300$ nm NLSV at the height ≈50 nm above the substrate at the peak of the broad maximum in dT/dx.

is critical for realistic modeling, we take the value ∼3 W/mK that we measure frequently for this Si-N using the suspended Si-N platforms [34], and use literature values for Si thermal conductivity (2000 W/mK at 78 K) [65]. For simplicity we use temperature-independent thermal conductivity (since most of these materials have k that varies slowly if at all over the few-kelvin range of heating we expect), and also make the simplifying assumption that all Joule heat is dissipated in the FM1 nanowire. In the case of Py (a high electrical resistivity alloy) and Al (a potentially low conductivity metal) with a truly clean interface and bulklike values of ρ this would likely be a poor assumption. However, the reduced size, impurity, and roughness and the likelihood of less-than-ideal contact all suggest that modeling this limit could be more realistic. Any spreading of the applied current to FM1 into the NM channel would cause some amount of the dissipated power to occur also in the NM, which would serve to reduce the thermal gradient calculated at the FM/NM interface. This would then increase the value of S_s estimated from the FEM model. Overall, this challenge falls in the realm of the difficulty all groups have with taking interface heat flow and thermal properties correctly into account when performing thermal modeling.

We set P_{2d} dissipated in FM1 by matching the temperature difference to that required to generate the measured voltage response at the FM2/NM thermocouple. The FEM problem is then solved using an adaptive mesh with >5000 nodes [as shown in Fig. 8(a)]. The resulting solution for $T(x,y)$ is shown in Fig. 8(b), and this solution is plotted for the height midpoint of the NM channel as a function of length along the channel in Fig. 8(c). The numerical derivative of this curve gives the thermal gradient dT/dx as a function of x as shown in Fig. 8(d). As expected this indicates somewhat smaller thermal gradients in the FM within one spin diffusion length of the interface compared to the analytic model. Note also that the thermal gradient vector at the FM/NM channel interface points toward the FM (in the negative x direction) for this device. The same operating conditions discussed above for the $L = 1300$ nm device at 78 K give $\nabla T_{\mathrm{FEM}} = 23$ K/μm. The same procedure applied to the 500 nm geometry gives a yet lower thermal gradient, which most likely indicates breakdown in the assumptions, and possibly that the relative Seebeck coefficients or thermal conductivities are in fact not the same between these devices.

To calculate S_s we then assume a value of $\lambda_{\mathrm{FM}} = 5$ nm for Py for easiest comparison to other work, though note that variation in this value directly affects S_s and that our results would be best discussed as the product $S_s\lambda_{\mathrm{FM}}$. Finally, we determine V_s via solution of the Valet-Fert equation using measured $V_s = R_2^s I^2$ at the detector junction, λ_{NM}, and L for each NLSV. The result (for $L = 1300$ nm) is $S_s = -0.5\ \mu$V/K (from the analytic method) and $S_s = -0.77\ \mu$V/K (from the FEM method) for our Py/Al at 78 K. This absolute value is somewhat smaller than other reports, which range from $S_s = -3.8\ \mu$V/K for Py/Cu at 300 K in the original report [15], to as large as $S_s = -72\ \mu$V/K for CoFeAl/Cu also at 300 K where the strong enhancement is believed to relate to formation of a half-metallic phase in the CoFeAl film [18]. However, viewed as a fraction of the T-dependent total absolute Seebeck coefficient of Py, S_{abs}^{Py}, in order to compare across the different measurement temperatures, our value $S_s/S_{\mathrm{abs}}^{Py} = 0.12$–$0.3$ is closer to (and perhaps even in excess of) that seen in other Py devices $S_s/S_{\mathrm{abs}}^{Py} = 0.19$ [15].

It is quite remarkable that the size of the thermal spin injection signals correspond to this very significant degree of polarization of the Seebeck coefficient when the interfacial current polarization, $P_I = 0.02$, determined from the size and L dependence of the electrical spin signal is so low. As stated above, we attribute the low electrical injection signals and P_I to a high degree of interfacial spin-flip scattering. Some reduction of the spin polarization α of the bulk of the Py itself could also contribute, though films made from this source in this chamber have historically not shown dramatically reduced values of M_s, anisotropic magnetoresistance, or of course

Seebeck coefficient [31,43,66]. The most likely cause for the reduced electrical spin injection is the formation of oxidized permalloy at the FM/NM junction that was not fully removed by the RF cleaning step before Al deposition. Native permalloy oxides can be complicated chemically and magnetically [67], though typically are not seen to develop long-range magnetic order above ∼30 K [68–70]. However, the permalloy oxide is a likely source of intermediate energy states in the barrier with random local magnetic environments that could easily contribute to loss of spin fidelity as initially spin-polarized electrons transport from Py to Al. Importantly, our large $S_s/S_{\rm abs}^{Py}$ values indicate that thermal injection suffers much less from this loss of signal due to interfacial effects.

Though it is not possible to clearly identify a physical origin of this reduced sensitivity to the interface based on results presented here, we point out that the physical processes involved in electrical and thermal injection are potentially quite different. This is particularly true when the clean interface limit is not achieved. While electrical spin injection in the limit of high R_c invokes tunneling of spin-polarized electrons, thermal injection in the tunneling limit could proceed by incoherent spin pumping as seen in the longitudinal spin Seebeck effect [71–82]. In this picture, the magnetic oxide could increase the effective interfacial spin mixing conductance or allow transport of spin via (nonelectronic) collective spin excitations [43,83–86]. Though the current devices are in an intermediate limit, these effects from excitation of collective magnetization could still contribute to the SDSE signal measured here. Further experiments exploring thermal spin injection in a range of materials and with more carefully controlled and characterized interfaces are required to clarify the potential advantages of thermal spin injection for a wide range of potential spintronic applications.

V. CONCLUSIONS

In summary, we presented evidence of thermally generated pure spin currents in permalloy/aluminum nonlocal spin valve structures. Electrical spin injection, combined with contact resistance and using the actual geometry of the nanoscale devices determined from SEM images, indicated relatively high resistance junctions and low values of interfacial spin polarization that we attribute to the presence of oxidized permalloy that remains at the FM/NM interface. Surprisingly, thermal spin injection remains efficient, suggesting that the oxidized permalloy participates in converting heat in the metallic FM into pure spin current in the NM, presumably via excitation of a collective magnetization. We also briefly discussed challenges in quantifying thermal gradients in nanoscale structures, and described two methods for estimating thermal gradients in the NLSV. We used these to quote a spin-dependent Seebeck coefficient in this Py/Al structure at 78 K near 1 μV/K, which agrees well with previous reports on Py/Cu structures at 300 K when compared as a fraction of the total absolute Seebeck coefficient.

ACKNOWLEDGMENTS

We thank C. Leighton, P. Crowell, and L. O'Brien for many helpful discussions on fabrication and physics of NLSVs, J. Aumentado for advice on EBL, G. C. Hilton, J. Beall, and J. Neibarger for advice and assistance on RF surface preparation and Al deposition, and J. Nogan and the IL staff at CINT for guidance and training. We gratefully acknowledge support from the DU PROF program (A.H.) as well as the NSF (Grants No. DMR-0847796 and No. DMR-1410247, D.W. and B.L.Z.). B.L.Z. also thanks the University of Minnesota Chemical Engineering and Materials Science Department, as a portion of this work benefited from support of the George T. Piercy Distinguished Visiting Professorship. This work was performed, in part, at the Center for Integrated Nanotechnologies, an Office of Science User Facility operated for the US Department of Energy (DOE) Office of Science by Los Alamos National Laboratory (Contract No. DE-AC52-06NA25396) and Sandia National Laboratories (Contract No. DE-AC04-94AL85000).

APPENDIX: ANALYTIC THERMAL MODELING OF NLSVs

For the case of electrical spin injection [Fig. 1(a)] in steady state with I applied to junction 1, we can write two coupled equations for heat flow:

$$P_J + P_\Pi = K_{\rm Sub}\left(T_1^e - T_0\right) + K_{\rm nm}\left(T_1^e - T_2^e\right), \tag{A1}$$

$$0 = K_{\rm Sub}\left(T_2^e - T_o\right) + K_{\rm nm}\left(T_2^e - T_1^e\right), \tag{A2}$$

where T_1^e (T_2^e) indicate the temperature of junction 1 (2) in response to power applied to junction 1 in the electrical spin injection configuration [Fig. 1(a)]. These can be solved to give the temperature differences between the junctions and the substrate:

$$T_2^e - T_0 = \frac{K_{\rm nm}(P_J + P_\Pi)}{K_{\rm sub}(K_{\rm sub} + 2K_{\rm nm})}, \tag{A3}$$

$$\Delta T_2^e = \frac{K_{\rm nm}\left(I^2 R_{\rm eff}^e + I S_{\rm rel} T_0\right)}{K_{\rm sub}(K_{\rm sub} + 2K_{\rm nm})} \tag{A4}$$

and

$$T_1^e - T_0 = \frac{P_J + P_\Pi}{K_{\rm Sub}} - \Delta T_2^e, \tag{A5}$$

$$\Delta T_1^e = \frac{I^2 R_{\rm eff}^e + I S_{\rm rel} T_0}{K_{\rm sub}} - \Delta T_2^e. \tag{A6}$$

This combination of Joule and Peltier power applied to junction 1 will lead to a voltage contribution from purely thermoelectric effects at junction 2, $V_{\rm NLE} = S_{\rm rel}\Delta T_2^e$. Equation (A4) clearly shows that this voltage will have terms proportional to both I and I^2, as seen in Figs. 5(a) and 6(b).

Similar expressions describe the device in the thermal spin injection configuration [Fig. 1(c)]. Here only Joule heating is expected, as shown in the thermal model schematic inset in Fig. 6(c), so that when current is driven through FM1,

$$P_J = K_{\rm Sub}\left(T_1^t - T_o\right) + K_{\rm nm}\left(T_1^t - T_2^t\right), \tag{A7}$$

$$0 = K_{\rm Sub}\left(T_2^t - T_o\right) + K_{\rm nm}\left(T_2^t - T_1^t\right). \tag{A8}$$

Here T_1^t (T_2^t) indicate the temperature of junction 1 (2) in response to power applied to FM1 in the thermal spin injection orientation [Fig. 1(c)].

Again these can be solved to give the temperature differences between the junctions and the substrate:

$$T_2^t - T_0 = \frac{K_{\rm nm}(P_J)}{K_{\rm sub}(K_{\rm sub} + 2K_{\rm nm})}, \tag{A9}$$

$$\Delta T_2^t = \frac{K_{\rm nm}\left(I^2 R_{\rm eff}^t\right)}{K_{\rm sub}(K_{\rm sub} + 2K_{\rm nm})} \tag{A10}$$

and

$$T_1^t - T_0 = \frac{P_J}{K_{\rm Sub}} - \Delta T_2^t, \tag{A11}$$

$$\Delta T_1^t = \frac{I^2 R_{\rm eff}^t}{K_{\rm sub}} - \Delta T_2^t. \tag{A12}$$

The Joule power applied to FM1 will again lead to a voltage contribution from purely thermoelectric effects at junction 2, $V_{\rm NLT} = S_{\rm rel}\Delta T_2^t$. As expected, the model predicts only $\propto I^2$ terms for $V_{\rm NLT}$, and the measurements [Figs. 5(b) and 6(d)] are indeed nearly perfect parabolas.

Finally, we note that the "contact resistance" measurement, where the voltage is measured at the FM strip used for current injection as shown in Fig. 6(e), will give the sum of potentially three voltages: a voltage drop caused by current flow across the actual interface between NM and FM1 (the traditional understanding of a contact resistance), a potential difference due to geometrical current spreading in the nanoscale circuit [9], and a voltage from thermoelectric effects due to the temperature gradients produced in the structure. This sum is then

$$V_C = I R_{\rm C} + V_{\rm spread} + S_{\rm rel}\Delta T_1^e. \tag{A13}$$

The thermoelectric voltage includes both I and I^2 terms, and as seen in Fig. 6(e) these IV curves show clear nonlinearity. It will also be important to consider the size of the thermoelectric term $\propto I$ relative to the average apparent resistance in using these effective 3-terminal measurements to judge which form of the 1d spin diffusion equation to choose for analysis of the spin transport in the NLSV [39]. In the NLSV devices shown here, the thermoelectric $\propto I$ term is small compared to the total signal [on the order of 100 nV for the measurement shown in Fig. 6(e)].

This model therefore provides expressions for three voltage measurements as a function of applied current with terms proportional to I and to I^2 as shown in Eqs. (7)–(9), where the A_i, B_i, and C_i coefficients result from fits to the measured V as a function of I as shown in Fig. 6. Measurements and fitting of these three voltages allows determination of the temperature profile in the device.

[1] M. Johnson, Phys. Rev. Lett. **70**, 2142 (1993).
[2] F. J. Jedema, A. T. Filip, and B. J. van Wees, Nature (London) **410**, 345 (2001).
[3] Y. Ji, A. Hoffmann, J. S. Jiang, and S. D. Bader, Appl. Phys. Lett. **85**, 6218 (2004).
[4] S. O. Valenzuela and M. Tinkham, Appl. Phys. Lett. **85**, 5914 (2004).
[5] Y. Niimi, D. Wei, H. Idzuchi, T. Wakamura, T. Kato, and Y. C. Otani, Phys. Rev. Lett. **110**, 016805 (2013).
[6] N. Tombros, C. Jozsa, M. Popinciuc, H. T. Jonkman, and B. J. van Wees, Nature (London) **448**, 571 (2007).
[7] X. Lou, C. Adelmann, S. A. Crooker, E. S. Garlid, J. Zhang, K. S. M. Reddy, S. D. Flexner, C. J. Palmstrom, and P. A. Crowell, Nat. Phys. **3**, 197 (2007).
[8] L. O'Brien, D. Spivak, J. S. Jeong, K. A. Mkhoyan, P. A. Crowell, and C. Leighton, Phys. Rev. B **93**, 014413 (2016).
[9] L. O'Brien, M. J. Erickson, D. Spivak, H. Ambaye, R. J. Goyette, V. Lauter, P. A. Crowell, and C. Leighton, Nat. Commun. **5**, 3927 (2014).
[10] M. Erekhinsky, A. Sharoni, F. Casanova, and I. K. Schuller, Appl. Phys. Lett. **96**, 022513 (2010).
[11] M. Yamada, D. Sato, N. Yoshida, M. Sato, K. Meguro, and S. Ogawa, IEEE Trans. Magn. **49**, 713 (2013).
[12] S. Kasai, S. Hirayama, Y. K. Takahashi, S. Mitani, K. Hono, H. Adachi, J. Ieda, and S. Maekawa, Appl. Phys. Lett. **104**, 162410 (2014).
[13] S. Hu and T. Kimura, Phys. Rev. B **87**, 014424 (2013).
[14] F. L. Bakker, A. Slachter, J.-P. Adam, and B. J. van Wees, Phys. Rev. Lett. **105**, 136601 (2010).
[15] A. Slachter, F. L. Bakker, J.-P. Adam, and B. J. van Wees, Nat. Phys. **6**, 879 (2010).
[16] F. Casanova, A. Sharoni, M. Erekhinsky, and I. K. Schuller, Phys. Rev. B **79**, 184415 (2009).
[17] M. Erekhinsky, F. Casanova, I. K. Schuller, and A. Sharoni, Appl. Phys. Lett. **100**, 212401 (2012).
[18] S. Hu, H. Itoh, and T. Kimura, NPG Asia Mater. **6**, e127 (2014).
[19] S. Hu and T. Kimura, Phys. Rev. B **90**, 134412 (2014).
[20] K. Yamasaki, S. Oki, S. Yamada, T. Kanashima, and K. Hamaya, Appl. Phys. Express **8**, 043003 (2015).
[21] A. Pfeiffer, S. Hu, R. M. Reeve, A. Kronenberg, M. Jourdan, T. Kimura, and M. Klaui, Appl. Phys. Lett. **107**, 082401 (2015).
[22] G.-M. Choi, C.-H. Moon, B.-C. Min, K.-J. Lee, and D. G. Cahill, Nat. Phys. **11**, 576 (2015).
[23] G. E. W. Bauer, E. Saitoh, and B. J. van Wees, Nat. Mater. **11**, 391 (2012).
[24] A. Hoffmann and S. D. Bader, Phys. Rev. Appl. **4**, 047001 (2015).
[25] L. Su, Y. Zhang, J.-O. Klein, Y. Zhang, A. Bournel, A. Fert, and W. Zhao, Sci. Rep. **5**, 14905 (2015).
[26] R. L. Stamps, S. Breitkreutz, J. Åkerman, A. V. Chumak, Y. Otani, G. E. W. Bauer, J.-U. Thiele, M. Bowen, S. A. Majetich, M. Kläui, I. L. Prejbeanu, B. Dieny, N. M. Dempsey, and B. Hillebrands, J. Phys. D **47**, 333001 (2014).
[27] B. Behin-Aein, D. Datta, S. Salahuddin, and S. Datta, Nat. Nanotechnol. **5**, 266 (2010).
[28] S. A. Wolf, D. D. Awschalom, R. A. Buhrman, J. M. Daughton, S. von Molnar, M. L. Roukes, A. Y. Chtchelkanova, and D. M. Treger, Science **294**, 1488 (2001).

[29] R. Sultan, A. D. Avery, G. Stiehl, and B. L. Zink, J. Appl. Phys. **105**, 043501 (2009).

[30] B. L. Zink, A. D. Avery, R. Sultan, D. Bassett, and M. R. Pufall, Solid State Commun. **150**, 514 (2010).

[31] A. D. Avery, R. Sultan, D. Bassett, D. Wei, and B. L. Zink, Phys. Rev. B **83**, 100401 (2011).

[32] A. D. Avery, M. R. Pufall, and B. L. Zink, Phys. Rev. B **86**, 184408 (2012).

[33] A. D. Avery and B. L. Zink, Phys. Rev. Lett. **111**, 126602 (2013).

[34] R. Sultan, A. D. Avery, J. M. Underwood, S. J. Mason, D. Bassett, and B. L. Zink, Phys. Rev. B **87**, 214305 (2013).

[35] A. D. Avery, S. J. Mason, D. Bassett, D. Wesenberg, and B. L. Zink, Phys. Rev. B **92**, 214410 (2015).

[36] Nanometer Pattern Generation System, http://www.jcnabity.com.

[37] White paper: New instruments can lock out lock-ins, 2005, Keithley Instruments, Inc., Cleveland, OH, http://www.tek.com/sites/tek.com/files/media/document/resources/Lock-In WP.pdf.

[38] A. Hojem, Thermal effects on spin currents in non-local metallic spin valves, Ph.D. thesis, University of Denver, 2016.

[39] S. Takahashi and S. Maekawa, Phys. Rev. B **67**, 052409 (2003).

[40] J. Bass and W. P. Pratt, J. Phys.: Condens. Matter **19**, 183201 (2007).

[41] A. Fert and S.-F. Lee, Phys. Rev. B **53**, 6554 (1996).

[42] Y. Fukuma, L. Wang, H. Idzuchi, S. Takahashi, S. Maekawa, and Y. Otani, Nat. Mater. **10**, 527 (2011).

[43] B. L. Zink, M. Manno, L. O'Brien, J. Lotze, M. Weiler, D. Bassett, S. J. Mason, S. T. B. Goennenwein, M. Johnson, and C. Leighton, Phys. Rev. B **93**, 184401 (2016).

[44] M. Isasa, E. Villamor, L. Fallarino, O. Idigoras, A. K. Suszka, C. Tollan, A. Berger, L. E. Hueso, and F. Casanova, J. Phys. D **48**, 215003 (2015).

[45] G. Mihajlovic, D. K. Schreiber, Y. Liu, J. E. Pearson, S. D. Bader, A. K. Petford-Long, and A. Hoffmann, Appl. Phys. Lett. **97**, 112502 (2010).

[46] S. Chen, C. Qin, and Y. Ji, J. Appl. Phys. **118**, 033901 (2015).

[47] D. G. Cahill, P. V. Braun, G. Chen, D. R. Clarke, S. Fan, K. E. Goodson, P. Keblinski, W. P. King, G. D. Mahan, A. Majumdar, H. J. Maris, S. R. Phillpot, E. Pop, and L. Shi, Appl. Phys. Rev. **1**, 011305 (2014).

[48] D. G. Cahill, W. K. Ford, K. E. Goodson, G. D. Mahan, A. Majumdar, H. J. Maris, R. Merlin, and S. R. Phillpot, J. Appl. Phys. **93**, 793 (2003).

[49] M. E. Siemens, Q. Li, R. Yang, K. A. Nelson, E. H. Anderson, M. M. Murnane, and H. C. Kapteyn, Nat. Mater. **9**, 26 (2010).

[50] K. T. Regner, J. P. Freedman, and J. A. Malen, Nanoscale Microscale Thermophys. Eng. **19**, 183 (2015).

[51] J. M. Larkin and A. J. H. McGaughey, Phys. Rev. B **89**, 144303 (2014).

[52] K. T. Regner, D. P. Sellan, Z. Su, C. H. Amon, A. J. H. McGaughey, and J. A. Malen, Nat. Commun. **4**, 1640 (2013).

[53] J. A. Johnson, A. A. Maznev, J. Cuffe, J. K. Eliason, A. J. Minnich, T. Kehoe, C. M. Sotomayor Torres, G. Chen, and K. A. Nelson, Phys. Rev. Lett. **110**, 025901 (2013).

[54] A. J. Minnich, J. A. Johnson, A. J. Schmidt, K. Esfarjani, M. S. Dresselhaus, K. A. Nelson, and G. Chen, Phys. Rev. Lett. **107**, 095901 (2011).

[55] F. K. Dejene, J. Flipse, and B. J. van Wees, Phys. Rev. B **90**, 180402 (2014).

[56] C. Strunk, M. Henny, C. Schönenberger, G. Neuttiens, and C. Van Haesendonck, Phys. Rev. Lett. **81**, 2982 (1998).

[57] G. Szakmany, A. Orlov, G. Bernstein, and W. Porod, IEEE Trans. Nanotechnol. **13**, 1234 (2014).

[58] S. J. Mason, Nanoscale thermoelectrics: A study of the absolute Seebeck coefficient of thin films, Ph.D. thesis, University of Denver, 2014.

[59] J. Flipse, F. L. Bakker, A. Slachter, F. K. Dejene, and B. J. van Wees, Nat. Nanotechnol. **7**, 166 (2012).

[60] W.-J. Lee, H. J. Kim, J. W. Kim, D. H. Nam, K.-Y. Choi, and K. H. Kim, Thermochim. Acta **603**, 244 (2015).

[61] C. Baldasseroni, D. R. Queen, D. W. Cooke, K. Maize, A. Shakouri, and F. Hellman, Rev. Sci. Instrum. **82**, 093904 (2011).

[62] Y. Anahory, M. Guihard, D. Smeets, R. Karmouch, F. Schiettekatte, P. Vasseur, P. Desjardins, L. Hu, L. Allen, E. Leon-Gutierrez, and J. Rodriguez-Viejo, Thermochim. Acta **510**, 126 (2010).

[63] B. Revaz, B. L. Zink, D. O'Neil, L. Hull, and F. Hellman, Rev. Sci. Instrum. **74**, 4389 (2003).

[64] MATLAB and Partial Differential Equations Toolbox Release 2009a, The MathWorks, Inc., Natick, Massachusetts, United States.

[65] C. J. Glassbrenner and G. A. Slack, Phys. Rev. **134**, A1058 (1964).

[66] D. Wesenberg, A. Hojem, and B. L. Zink (unpublished).

[67] M. R. Fitzsimmons, T. J. Silva, and T. M. Crawford, Phys. Rev. B **73**, 014420 (2006).

[68] K. O'Grady, S. Greaves, and S. Thompson, J. Magn. Magn. Mater. **156**, 253 (1996).

[69] S. H. Charap and E. Fulcomer, J. Appl. Phys. **42**, 1426 (1971).

[70] S. B. Bailey, T. M. Peterlin, R. T. Richard, and E. N. Mitchell, J. Appl. Phys. **41**, 194 (1970).

[71] D. Meier, D. Reinhardt, M. van Straaten, C. Klewe, M. Althammer, M. Schreier, S. T. B. Goennenwein, A. Gupta, M. Schmid, C. H. Back, J.-M. Schmalhorst, T. Kuschel, and G. Reiss, Nat. Commun. **6**, 8211 (2015).

[72] S. M. Wu, F. Y. Fradin, J. Hoffman, A. Hoffmann, and A. Bhattacharya, J. Appl. Phys. **117**, 17C509 (2015).

[73] S. M. Rezende, R. L. Rodriguez-Suarez, J. C. Lopez Ortiz, and A. Azevedo, Phys. Rev. B **89**, 134406 (2014).

[74] K.-i. Uchida, T. Kikkawa, A. Miura, J. Shiomi, and E. Saitoh, Phys. Rev. X **4**, 041023 (2014).

[75] K. Uchida, M. Ishida, T. Kikkawa, A. Kirihara, T. Murakami, and E. Saitoh, J. Phys.: Condens. Matter **26**, 343202 (2014).

[76] A. Kehlberger, G. Jakob, M. C. Onbasli, D. H. Kim, C. A. Ross, and M. Kläui, J. Appl. Phys. **115**, 17C731 (2014).

[77] D. Qu, S. Y. Huang, J. Hu, R. Wu, and C. L. Chien, Phys. Rev. Lett. **110**, 067206 (2013).

[78] M. Schreier, A. Kamra, M. Weiler, J. Xiao, G. E. W. Bauer, R. Gross, and S. T. B. Goennenwein, Phys. Rev. B **88**, 094410 (2013).

[79] M. Weiler, M. Althammer, F. D. Czeschka, H. Huebl, M. S. Wagner, M. Opel, I.-M. Imort, G. Reiss, A. Thomas, R. Gross, and S. T. B. Goennenwein, Phys. Rev. Lett. **108**, 106602 (2012).

[80] D. Meier, T. Kuschel, L. Shen, A. Gupta, T. Kikkawa, K. Uchida, E. Saitoh, J.-M. Schmalhorst, and G. Reiss, Phys. Rev. B **87**, 054421 (2013).

[81] R. Ramos, T. Kikkawa, K. Uchida, H. Adachi, I. Lucas, M. H. Aguirre, P. Algarabel, L. Morelln, S. Maekawa, E. Saitoh, and M. R. Ibarra, Appl. Phys. Lett. **102**, 072413 (2013).

[82] K.-i. Uchida, H. Adachi, T. Ota, H. Nakayama, S. Maekawa, and E. Saitoh, Appl. Phys. Lett. **97**, 172505 (2010).
[83] C. Hahn, G. de Loubens, V. V. Naletov, J. B. Youssef, O. Klein, and M. Viret, Europhys. Lett. **108**, 57005 (2014).
[84] H. Wang, C. Du, P. C. Hammel, and F. Yang, Phys. Rev. Lett. **113**, 097202 (2014).
[85] Y. Shiomi and E. Saitoh, Phys. Rev. Lett. **113**, 266602 (2014).
[86] M. E. Lucassen, C. H. Wong, R. A. Duine, and Y. Tserkovnyak, Appl. Phys. Lett. **99**, 262506 (2011).